RESEARCH PAPER

Probing start-up electroosmotic forces and flows in a microfluidic channel using laser tweezer force spectroscopy

A. Raudsepp[1] · S. B. Hall[1] · M. A. K. Williams[1,2]

Abstract

Transient displacements of optically trapped particles in [NaCl] = 0.1 mM solutions produced by electroosmotic and electrophoretic forces at electric field start-up were profiled wall-to-wall through 50 μm in a commercial microfluidic channel with a spatial resolution of 1 μm and temporal resolution of 200 kHz. Data were inverted to compute the force on the particles and fitted to a first-principles finite element methods model to compute the flow profile, and zeta potential of the walls and particles. This analysis suggested that (1) electroosmotic flow in the channel was accompanied by a pressure gradient, producing backflow, and which was attributed to bubbles within the channel and that (2) while the zeta potential of the wall was broadly consistent with that expected, the zeta potentials across the nine particles examined was higher than might be expected, which were attributed to differences in surface conditions of the particular particles used.

Keywords Optical tweezers · Microfluidics · Electroosmotic flow · Finite element methods

1 Introduction

Since their advent in the 1990's, microfluidic devices have become an increasingly popular platform for a wide range of scientific applications (Nge et al. 2013). Fluid transport in these devices can be an important design consideration. More commonly, fluid is moved through the channels of the device using a pressure gradient. While this approach can be simple, it has an important limitation: the flow profile across the channel is generally Poiseuille-like which results in Taylor dispersion (Aris 1956; Kirby 2010). Less commonly, an electric field is used to steer fluid in the device. Flow produced by an electric field in this way is called electroosmotic flow (EOF). By contrast to pressure-driven flow, EOF can be plug-like and does not suffer from Taylor

✉ A. Raudsepp
A.Raudsepp@massey.ac.nz

S. B. Hall
S.B.Hall@massey.ac.nz

M. A. K. Williams
M.Williams@massey.ac.nz

[1] School of Fundamental Sciences, Massey University, Palmerston North 4442, New Zealand

[2] MacDiarmid Institute for Advanced Materials and Nanotechnology, Wellington 6140, New Zealand

dispersion, which can be advantageous if this dispersion is to be avoided (Kirby 2010).

EOF is due to an interaction of the applied electric field with charged counter-ions near the channel's wall. In a fluid-filled channel, charges embedded in the wall lead to a separation of charge in solution and the formation of a diffuse layer of oppositely charged counter-ions near the wall's surface. An electric field produces an electrophoretic force on these counter-ions, inducing movement. Momentum associated with this movement diffuses out from this layer into the fluid, resulting in plug-like flow at long times. The evolution of the flow profile that occurs on the application of the field at start-up, from flow at the walls at short times, to plug-like at long times, can be very rapid. Charged species in suspension will also experience an electrophoretic force. This force can induce movement relative to the background EOF, and this relative motion is the basis of electrokinetic separation and capillary electrophoresis (Hunter 2001; Kirby 2010).

Because of the speed at which EOF develops, very high time resolution is required to monitor the time evolution of the flow profile at start-up. Considerable progress towards an experimental understanding of EOF has been achieved using particle imaging velocimetry (PIV). In this method, the fluid is seeded with particles and the flow profile is inferred by comparing pairs of triggered images separated in time using cross correlation. Results are generally consistent with that

predicted (Yan et al. 2006; Sureda et al. 2012; Miller et al. 2015). Because the flow is inferred from the motion of multiple particles, which themselves may have variable electrophoretic behaviour, there is potentially some ambiguity in these measurements, and the time response of the method is limited by the exposure time required to image the particles.

Laser tweezer force spectroscopy can potentially address some of the limitations of PIV. In laser tweezer force spectroscopy the force on a single optically trapped particle is inferred from its displacement from equilibrium. With appropriate detection, very high time resolution is possible. A disadvantage of the approach is that the method is only sensitive to forces at the location of the particle, and the particle must be sequentially stepped through the channel to profile the flow. Laser tweezer force spectroscopy has been used to examine both flow and the particle's electrophoretic properties in the frequency domain by applying a sinusoidally time-varying electric field and monitoring the steady state amplitude and phase of the resulting displacement (Semenov et al. 2009; Kahl et al. 2009; van Heiningen et al. 2010). This approach can be used to infer start-up flow, however, it is somewhat indirect.

The time evolution of the EOF profile can be calculated by solving the Navier–Stokes/Cauchy momentum equation in conjunction with the Poisson equation (Kirby 2010). Because of the complexity associated with solving this pair of coupled partial differential equations (PDE), analytic investigations have historically been limited to simpler cases (Keh and Tseng 2001; Marcos et al. 2004; Chang and Wang 2008). Numerical approaches based on finite element methods (FEM) can be used to model more complex situations, and recent innovations in software design have improved the accessibility of FEM, making this approach increasingly practical (Zhao et al. 2017).

In this study, we use a commercially available microfluidic device and EOF set-up, with conventional laser tweezers, and commercial FEM tools, to investigate start-up forces and flows in a microfluidic channel in the time domain. We begin by backgrounding the relevant theory, and follow describing the set-up, and experimental results. As will be seen, the start-up flow is more complex than would be naively predicted and suggests that the EOF is accompanied by a pressure gradient.

2 Background

In Zhao et al. (2017), the Authors develop a description of electroosmotic flow of a non-Newtonian fluid in a rectangular channel. For clarity, we give these results for a Newtonian fluid here. Following Zhao et al. (2017), the electric potential, V, and electroosmotic flow velocity, $\mathbf{u} = u\hat{x}$ of a Newtonian fluid, within an infinitely long rectangular channel of width

$2W$ (y-direction) and height $2H$ (z-direction) and centered on the origin, generated by an electric field $\mathbf{E}(t) = E(t)\hat{x}$ are governed by non-dimensionalized Poisson, and Navier–Stokes equations:

$$\frac{\partial^2 V'}{\partial y'^2} + \frac{\partial^2 V'}{\partial z'^2} = K^2 \sinh V', \tag{1}$$

$$\frac{\partial u'}{\partial t'} = \frac{\partial^2 u'}{\partial y'^2} + \frac{\partial^2 u'}{\partial z'^2} - E'(t)K^2 \sinh V' + \frac{\mathrm{d}p'}{\mathrm{d}x'}, \tag{2}$$

where:

$$D_{\mathrm{h}} = \frac{4WH}{W+H}, \quad x' = \frac{x}{D_{\mathrm{h}}}, \quad y' = \frac{y}{D_{\mathrm{h}}}, \quad z' = \frac{z}{D_{\mathrm{h}}},$$

$$V' = \frac{z_{\mathrm{v}}e}{k_{\mathrm{B}}T}V, \quad K = \kappa D_{\mathrm{h}}, \quad u' = \frac{\eta D_{\mathrm{h}}(z_{\mathrm{v}}e)^2}{\varepsilon_0\varepsilon_{\mathrm{r}}(k_{\mathrm{B}}T)^2}u,$$

$$t' = \frac{\eta}{\rho D_{\mathrm{h}}^2}t, \quad E'(t) = \frac{z_{\mathrm{v}}eD_{\mathrm{h}}}{k_{\mathrm{B}}T}E(t), \quad p' = \frac{D_{\mathrm{h}}^3}{k_B T}p.$$

Here, D_{h} is the channels hydraulic diameter, z_{v} is the valence of charge carrier ($z_{\mathrm{v}} = 1$ is assumed in all calculations), $e = 1.602 \times 10^{-19}$ C is the elementary charge, $k_{\mathrm{B}} = 1.38 \times 10^{-23}$ J/K is Boltzmann's constant, T is the temperature ($T = 293$ K is assumed), $\varepsilon_0 = 8.85 \times 10^{-12}$ F/m is the permittivity of free space and ε_{r} the relative permittivity ($\varepsilon_{\mathrm{r}} = 78.5$ is assumed), and η and ρ are the fluids viscosity and density ($\rho = 1000$ kg/m^3 assumed). $\kappa^{-1} = [\varepsilon_0\varepsilon_{\mathrm{r}}k_{\mathrm{B}}T/(2e^2 z_{\mathrm{v}}^2 n_\infty)]^{1/2}$ is the Debye length, where n_∞ is the number density of charge carriers in the fluid ($n_\infty = 6.022 \times 10^{20}$ m^{-3} is assumed for [NaCl] = 0.1 mM used experimentally, giving an assumed Debye length $\kappa^{-1} = 30$ nm). Finally, p is the pressure so that $\mathrm{d}p'/\mathrm{d}x'$ is a non-dimensionalized pressure gradient (which will be assumed to be zero, unless noted otherwise). The coupled pair of PDE described by Eqs. 1 and 2 are solved subject to the boundary conditions:

$$\left.\frac{\partial V'}{\partial y'}\right|_{\pm W/D_{\mathrm{h}}} = \left.\frac{\partial V'}{\partial z'}\right|_{\pm H/D_{\mathrm{h}}} = \frac{z_{\mathrm{v}}e}{k_{\mathrm{B}}T}\zeta_{\mathrm{w}}, \tag{3}$$

$$\left.\frac{\partial u'}{\partial y'}\right|_{\pm W/D_{\mathrm{h}}} = \left.\frac{\partial u'}{\partial z'}\right|_{\pm H/D_{\mathrm{h}}} = 0, \tag{4}$$

where ζ_{w} is the wall zeta potential, and initial conditions:

$$\left.u'\right|_{t'=0} = 0. \tag{5}$$

These equations were solved in COMSOL (using coefficient form PDE's). To verify our approach, we repeat calculations in Zhao et al. (2017), computing the mid-gap start-up flow profile $u'(y' = 0, z', t')$ in a $2W \times 2H = 15 \times 10\,\mu$m channel with wall zeta potential $\zeta_{\mathrm{w}} = -25$ mV, following
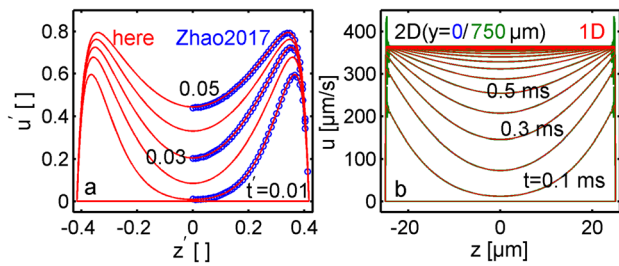
Fig. 1 **a** Comparison of flow profile calculated here with a literature calculation (Zhao et al. 2017). **b** Comparison of flow profiles calculated in 2D and 1D
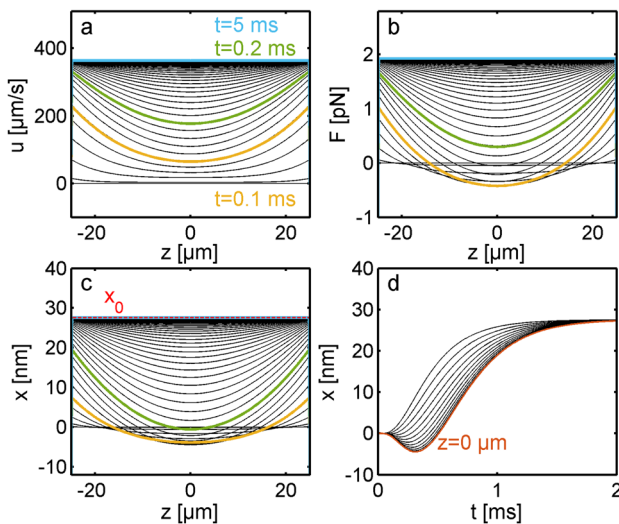

Fig. 2 **a** Calculated flow $u(z, t)$, **b** forces on an optically trapped particle and **c** and **d** associated displacement of the particle

the instantaneous application of an electric field in the positive x-direction. A comparison between Zhao et al. (2017) calculations (extracted from Fig. 2 of Zhao et al. 2017) and our calculations is shown in Fig. 1a. As demonstrated in the figure, the two results agree well verifying the accuracy of our calculation. Note that the flow is directed in the positive x-direction when the field is directed in the positive x-direction and ζ_w is negative (that is, the fluid flows from the positive to the negative electrode).

For much of the experimental work carried out here, a channel with dimensions $2W \times 2H = 1500 \times 50 \, \mu m$ was used. Calculated flows for this geometry assuming $\zeta_w = -50 \, mV$ and $E(t) = E_0(1 - \exp[-t/\tau])$, with $E_0 = 10,000 \, V/m$ and $\tau = 0.1 \, ms$ are shown in Fig. 1b. Here the flow is profiled at $u(y = 0 \, \mu m, z, t)$, $u(y = 375 \, \mu m, z, t)$ and $u(z, t)$. $u(z, t)$ is computed by neglecting the y dependence in Eqs. 1–2 and is a 1D calculation. These three sets of profiles are almost identical indicating that the flow profile is insensitive to y variation about $y = 0$ and that the 1D calculation can be used near $y \approx 0$. The 1D calculation is around 20 time faster than the 2D

calculation, which is an important consideration when fitting data, and all other calculations presented here are computed in 1D.

In laser tweezers force spectroscopy, force is inferred from measured displacement of an optically trapped particle (Jones et al. 2015). To relate force to displacement, an equation of motion is required. A particle suspended in electroosmotic flow will experience an electroosmotic drag force due to this motion of the fluid:

$$F_{EO} = \gamma u, \tag{6}$$

where γ is a drag constant. In addition, the particle will experience an electrophoretic force due to surface charge:

$$F_{EP} = \gamma \mu E = \gamma(\varepsilon \zeta_p / \eta)E, \tag{7}$$

where μ is the electrophoretic mobility of the particle and ζ_p is the particles zeta potential. The forces F_{EO} and F_{EP} will displace an optically trapped particle. In frequency space, the equation of the motion, or Langevin equation, for the displacement $\hat{x}$ of a particle with mass m and radius a, in a fluid of density ρ and viscosity η, trapped in an optical trap of stiffness k, and subject to electroosmotic $\hat{F}_{EO} = \gamma \hat{u}$, electrophoretic $\hat{F}_{EP}$ and Brownian forces $\hat{F}_B$ is:

$$\hat{F}_{EP} + \gamma \hat{u} + \hat{F}_B = k\hat{x} + i\omega \gamma \hat{x} - \omega^2 m\hat{x}, \tag{8}$$

where $\gamma = \gamma_0(1 + \alpha)$. $\gamma_0 = 6\pi\eta a$ is Stokes' Law and $\alpha = (1 + i)a\sqrt{\frac{\omega\rho}{2\eta}} + i\frac{\omega\rho a^2}{9\eta}$ and is related to the inertia of fluid displaced by the particle (van Heiningen et al. 2010). The contribution of the mass term is only relevant at very high frequencies (100 kHz+) and is neglected here. The contribution of the inertia term can be neglected if $\alpha \ll 1$. At 18 kHz (which corresponds to the reciprocal of the minimum characteristic time $\tau = 0.057 \, ms$ required to apply the field in the experimental set-up used here) and assuming $\eta = 1 \, mPa \, s$, $\rho = 1000 \, kg/m^3$ and $a = 500 \, nm$ (comparable to the radius of the particles used), $|\alpha| = 0.17 \ll 1$; because this is small here, the contribution of this term will be neglected also.

In the time domain, neglecting mass and fluid inertia terms, and neglecting any frequency dependence of μ (and ζ_p), the equation of motion is:

$$\gamma_0 u(t) + \gamma_0 \mu E(t) + F_B = kx(t) + \gamma_0 \frac{dx(t)}{dt}. \tag{9}$$

If Brownian motion and trap stiffness are neglected ($F_B = 0$ and $k = 0$) equation of motion Eq. 9 simplifies to an equation of motion:

$$u_{EP}(t) + u_{EO}(t) = \frac{dx}{dt} \tag{10}$$

where $u_{EP}(t) = \mu E(t)$ is the electrophoretic contribution to the particles velocity and $u_{EO}(t) = u(t)$ is the electroosmotic

contribution. If $x(t)$, in Eq. 9, is measured, and k and γ_0 are known, the force $F(t)$ on the particle can be calculated numerically:

$$F(t) = kx(t) + \gamma_0 \frac{\mathrm{d}x(t)}{\mathrm{d}t}. \tag{11}$$

Conversely, if $F(t)$ is known, $x(t)$ can be calculated numerically:

$$x(t) = \exp[-kt/\gamma_0] \int_{t'=0}^{t'=t} F(t') \exp[+kt'/\gamma_0]\mathrm{d}t'. \tag{12}$$

The relationship between $x(z, t)$ and $F(z, t)$ is illustrated with analytic data in Fig. 2. We assume that the applied field is $E(t) = E_0(1 - \exp[-t/\tau])$, with $E_0 = 10{,}000$ V/m and $\tau = 0.1$ ms, $\zeta_w = -50$ mV and $\zeta_p = -20$ mV, and $k = 70$ pN/µm. The resulting transient electroosmotic flow velocity $u(z, t)$, calculated in COMSOL, and $F(z, t) = \gamma_0(\varepsilon\zeta_p/\eta)E(t) + \gamma_0 u(z, t)$, calculated in MATLAB, are shown in Fig. 2a, b. $x(z, t)$ is calculated from $F(z, t)$ using Eq. 12 and the associated space time dependence of $x(z, t)$ is shown in Fig. 2c, d. Over most of the gap $x(t)$ (and $F(t)$) are roughly biexponential with an electrophoretic 'fast' mode and an electroosmotic 'slow' mode. Note that if ζ_p and ζ_w have the same sign, the electroomostic and electrophoretic forces on the particle are in opposite directions. At long times, $E(t) = E_0$ and $\mathrm{d}x/\mathrm{d}t = \mathrm{d}F/\mathrm{d}t = 0$ so that $F = kx_0$. Consequently:

$$\gamma_0(\varepsilon\zeta_p/\eta)E_0 - \gamma_0(\varepsilon\zeta_w/\eta)E_0 = kx_0 \tag{13}$$

so that:

$$\zeta_p - \zeta_w = \Delta\zeta = \varepsilon\eta k x_0/\gamma_0. \tag{14}$$

If x_0 can be estimated from the long time behavior, the difference between the zeta potential of particle and wall, $\Delta\zeta$, can be determined.

In the analytic description above, the effects of Brownian motion were neglected. To consider these effects, we assume that $F_{EO} = A_s(1 - \exp[-t/\tau_s])$, $F_{EP} = A_f(1 - \exp[-t/\tau_f])$ and $F_B(t)$ is drawn from a Gaussian distribution (with a positional variance comparable to that observed experimentally) so that:

$$A_s(1 - \exp[-t/\tau_s]) + A_f(1 - \exp[-t/\tau_f]) + F_B(t)$$
$$= kx(t) + \gamma_0 \frac{\mathrm{d}x(t)}{\mathrm{d}t}. \tag{15}$$

This equation was solved numerically to calculate $x(t)$. A solution to this equation, calculated using an explicit forth order Runge–Kutta method, is illustrated in Fig. 3a. As $F(t)$ depends on $\mathrm{d}x/\mathrm{d}t$, the calculated $F(t)$ can be expected to be very noisy. Also shown in this figure is an average solution over 250 runs and the solution when $F_B(t) = 0$. Here it can be seen that this average solution converges to the solution
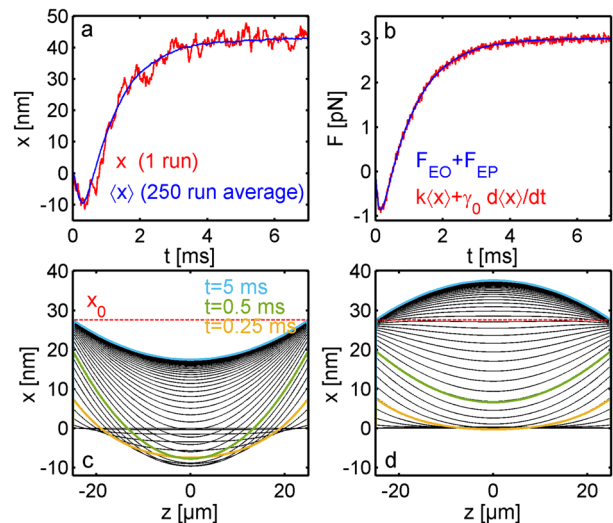

Fig. 3 **a** Effects of Brownian motion on $x(t)$ and on average $\langle x(t)\rangle$ and **b** effect on the resulting $F(t)$. Effect of negative **c** and positive **d** pressure gradient on $x(z, t)$

to $F_B(t) = 0$. Computing $F(t)$ from this averaged $x(t)$ gives $F_{EO} + F_{EP}$ as illustrated in Fig. 3b.

The effect of a pressure gradient on flow, $u(z, t)$, was also neglected in the earlier calculations. Because it will have some bearing on the interpretation of experimental data we repeat the calculation shown in Fig. 2c with a pressure gradient:

$$\frac{\mathrm{d}p'}{\mathrm{d}x'} = c_0 \tag{16}$$

where c_0 is a positive or negative constant. These calculations are shown in Fig. 3c, d. This pressure gradient perturbs the flow at all times, producing a deflection about x_0 at long times of the form:

$$x(z) = c_0'(z - H)^2 + x_0. \tag{17}$$

This is a potentially useful observation, as it indicates that a fit to the long time behavior can be used to determine x_0 and $\Delta\zeta$ (from Eq. 14), even if the short time behavior is not well understood.

3 Set-up

The experimental set-up used is illustrated in Fig. 4. Flow was principally examined in the central region of a 4 cm × 1500 µm × 50 µm ($L \times W \times H$) channel in a Micronit FLC50 thin bottom glass flow cell (chip) mounted in a Micronit EOF Kit 9015 holder (holder). Some additional measurements were made in the 4 cm × 1000 µm × 50 µm and 4 cm × 500 µm × 50 µm channels, that were also
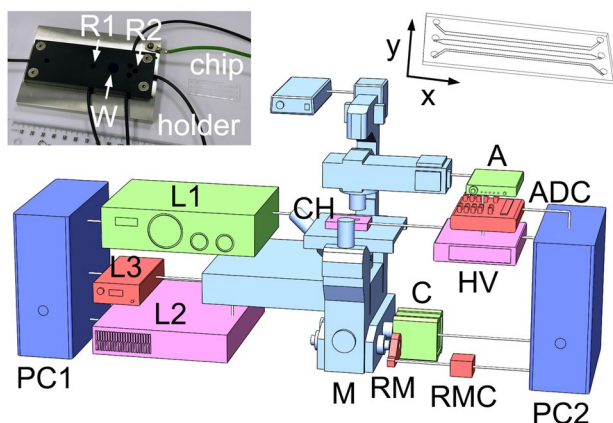
Fig. 4 Experimental set-up. A microfluidic chip is mounted (CH) on optical tweezers comprised of an inverted microscope (M, H), lasers (L1, L2, L3), automation and controller hardware (ADC, PC1, PC2, RMC, RM) and detectors and associated electronics (C, QPD, A) which are used to monitor the displacement of an optically trapped particle on the application of a high voltage (HV). See text for a more detailed description

available on this chip (after modifying the set-up to enable access for visualization of these side channels). This holder clamps the channel between two open reservoirs (R1 and R2) which can be connected via integrated electrodes to a high voltage source. This holder's top surface was modified with a window (W) so that the central region of the channel could be observed from above. The chip and holder (CH) was mounted on the stage of a modified Nikon Eclipse TE-2000 inverted microscope equipped with a fixed 5 W $\lambda = 1030$ nm Spectra Physics trapping laser, an SLM steered 2 W $\lambda = 1064$ nm Spectra Physics trapping laser and a 3 mW $\lambda = 650$ nm probe laser which were all focused using a Nikon 60×, NA = 1.2 water immersion objective, into the channel. The trapping lasers can be used to optically trap and position particles within the channel. The probe laser is focused onto the trapped particle and the forward scattered interference pattern produced focused by the microscope's condenser onto a quadrant photo-diode (QPD). Displacements of the particle produce a difference voltage across a pair of quadrant photo-diode sensors which is amplified (A). The relationship between this amplified difference voltage and displacement of the trapped particle (for each particle used and at all z-positions within the channel probed) was determined by stepping the position of the particle through the probe laser using the steerable $\lambda = 1064$ nm trap. All EOF measurements were conducted with the fixed $\lambda = 1030$ nm laser at a set laser power of 1.0 W. The z-position of the trapped particle (relative to the chip) was controlled via a motorized rotary mount (RM) and rotary mount controller (RMC) which was used to translate the objective and associated optical trap in the z-direction. Additional bright field imaging of the trapped particle was

conducted using an Andor NEO camera (C). Measurements were coordinated using a custom LabVIEW script in conjunction with a National Instrument Multifunction I/O USB-6361 (ADC) which was connected to the input of a Trek 601C high voltage amplifier (HV), the output of the QPD amplifier and rotary mount controller (RMC). This multifunction ADC device sent the desired waveform to the high voltage amplifier while acquiring a resulting signal from the QPD, sequentially stepping the optical trap through the channel. Both ADC output and input were synchronously sampled at 200 kHz.

Before each series of measurements, the glass chip was mounted in a Micronit Fluidic Connect Pro and the channel was slowly washed with 3 mL of Agilent Technologies HPCE 1 M Sodium Hydroxide over 10 min and then thoroughly rinsed with 10 mL of MQ deionized water. The sample, a dispersion of diameter $2a = 990$ nm Polyscience Polystyrene beads at a volume fraction 2×10^{-8} in ultrasonically degassed [NaCl] = 0.1 mM solution (pH 6.8) was loaded into the chip. At this very low salt concentration, Joule heating is expected to be negligible (Tang et al. 2006). The loaded chip was then mounted in the holder and 50 μL of [NaCl] = 0.1 mM suspension was added to each of the open reservoirs.

4 Results

The high voltage waveform applied to the sample, as measured at the output of the high voltage amplifier (through a high voltage divider), is shown in Fig. 5a with an expanded view of the region of interest (ROI) in Fig. 5b. The voltage steps between 0, 400, 0 and −400 V over 50 ms which produces corresponding fields of ±400 V/4 cm = ±10,000 V/m along the channel. This waveform was chosen to avoid progressively shunting the fluid into one reservoir over time which could be expected to produce a pressure gradient and back-flow. The rise time of the waveform was controlled in software. Listed in figures is a characteristic time τ_E of a real-time software convolution filter used to produce the waveform shown. Table 1 lists τ_E, and an approximate characteristic rise time τ, determined by fitting the data to a function of the form $V(t) = V_0(1 - \exp[-(t - t_0)/\tau])$. A high precision analytic approximation to the measured $V(t)$ was used in the COMSOL calculations.

After loading, a particle was located and optically trapped in a fixed $\lambda = 1030$ nm trap. The channel was translated so that $y \approx 0$ (that is, the particle was halfway between the sidewalls of the channel) and the particle was transferred to an aligned steerable trap. After aligning the probe laser (once) the steerable trap containing the particle the was swept back and forth through $\Delta x = 1200$ nm while the QPD voltage was monitored, and the particle was progressively stepped
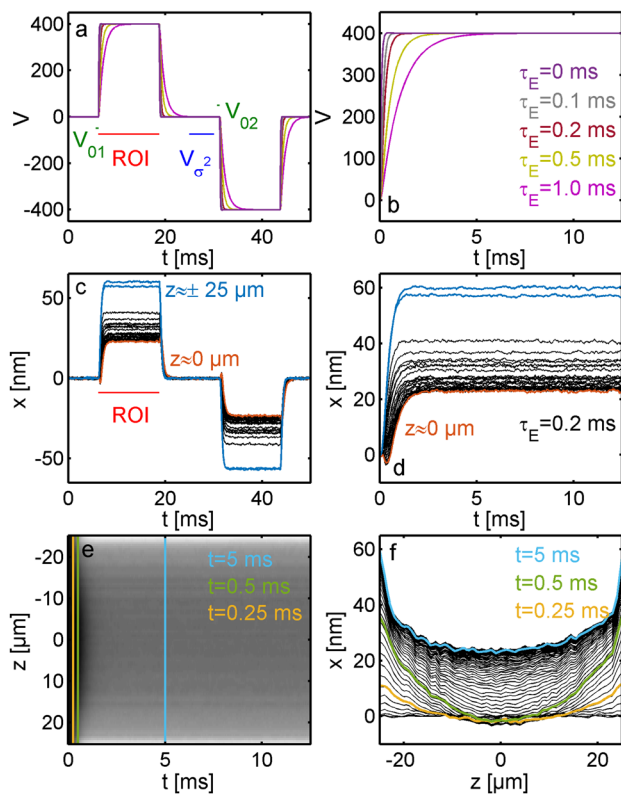
Fig. 5 a Measured output of the high voltage amplifier with **b** expanded view. **c** Resulting x-displacement of an optically trapped particle at $51 \times z$ displacements spanning the channel with **d** expanded view. **e** data in **d** mapped to surface. **f** Constant time x-displacements, as a function of z-position, within the gap (data is only shown at $\Delta t = 0.04$ ms increments for clarity)

Table 1 Characteristic time τ_E of a convolution filter used to modify the high voltage waveform and measured characteristic rise time τ of the high voltage $V(t)$ applied to the chip

τ_E (ms)	τ (ms)
0	0.057
0.1	0.14
0.2	0.22
0.5	0.50
1	1.0

through the gap in the z-direction in $\Delta z = 1$ μm increments from the lower to the upper walls of the channel. These measurements were used to determine a QPD calibration factor c_V. Typically, $c_V \approx 300$ nm/V. Experimentally, this calibration factor was found to be insensitive to z-position and a single average c_V was assumed in all calculations. Following calibration, the particle was transferred back into the fixed $\lambda = 1030$ nm trap and the time-varying high voltage applied to the sample as the particle was stepped in $\Delta z = 1$ μm increments through the gap. At each z-position, the QPD difference voltage $V(t)$ was acquired synchronously with the time-varying high voltage waveform, over 250

periods, and the period average $V(t)$ and variation about the average V_{σ^2} (over the times indicated in Fig. 5a) recorded. The displacement $x(t)$ was calculated according to:

$$x(t) = (k/k') \times c_V \times [V(t) - (V_{01} + V_{02})/2]. \quad (18)$$

The alignment of the probe laser and fixed trapping laser were not perfect and the probe and particle separated by a few tens of nm over $\Delta z = 50$ μm; the last term depending on the averages V_{01} and V_{02} (over the times indicated Fig. 5a) are included to account for this. Variations in trap stiffness k, with z, will directly affect the measured x. By contrast to c_V, k does vary slightly through the gap (discussed below). The prefactor k/k' is included to account for this variation. Here k is the gap average stiffness, which is assumed be $k = 70$ pN/μm in all calculations, and k' is a local stiffness which is calculated from V_{σ^2} using the equipartition principle.

The resulting displacement $x(t)$ of an optically trapped particle for $\tau_E = 0.2$ ms at $51 \times \Delta z$ steps, spanning the gap, is shown in Fig. 5c with an expanded view over the region of interest in Fig. 5d. The total acquisition time for this set of measurements was approximately 12 min. The particle is displaced opposite to the direction of the field at short times, over at least part of the gap, and in the direction of the field at longer times, with a steady-state displacement achieved in a few ms. The directionality of this displacement was verified using high-speed imaging. The data reported in Fig. 5d is mapped to a 2D surface, shown in Fig. 5e and profiles across this surface, at $\Delta t = 0.04$ ms increments, are given in Fig. 5f, to better show the spatial variation across the gap. Notably, the displacement of the particle is not constant across the gap at long times indicating that pure plug-like flow is not present.

To compute the force $F(t)$ from the displacement $x(t)$, using Eq. 11, the trap stiffness k and Stokes drag constant $\gamma_0 = 6\pi\eta a$, which depends on the effective viscosity η, must be determined within the channel. Both parameters are potentially sensitive to wall effects. To investigate, the restricted diffusion of a trapped particle was examined by recording both the particle's x-displacement power spectral density (PSD) and particle's image as the particle was stepped in $\Delta z = 100$ nm or $\Delta z = 500$ nm increments near the walls. When the channel's walls come in contact with the particle it displaces it, modifying the image statistics, which can be used to determine the z-displacement from the wall (Hansen et al. 2005; Raudsepp et al. 2015). Both k and η can be determined by considering the low- and high-frequency variation of the PSD (Berg-Sørensen and Flyvbjerg 2014; Raudsepp et al. 2018). Measured k is shown in Fig. 6a. While k does not show clear systematic variation near the walls, it does vary by around 5% throughout the gap about an average value $k = 70$ pN/μm. This variation
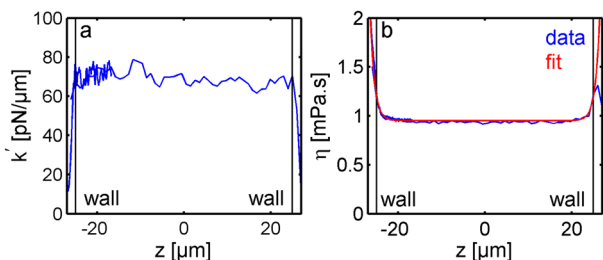
Fig. 6 a Measured optical trap stiffness k. **b** Measured viscosity η with fit

may be due to back reflections of the trapping laser from the parallel glass walls of the channel. By contrast to k, η does show some systematic variation near the wall but varies less within the gap, as illustrated in Fig. 6b. The data are well described by a function $\eta = \eta_0[1 + d_0 \cosh(z/d)]$ with $\eta_0 = 0.95$ mPa s, $d_0 = 7 \times 10^{-12}$ and $d = 1$ µm. The characteristic length d is small and within the absolute uncertainty to which z was determined in the measurements and because of this $\eta = \eta_0 = 0.95$ mPa s was assumed in all calculations.

In total, nine particles, loaded separately, were examined in a $2W = 1500$ µm channel. The displacements $x(z, t)$ for three of these particles at five τ_E values are shown in Fig. 7 1–15. The displacements vary between particles and with τ_E. τ_E effects the short time behavior, but has less of an effect on the long time behavior. Measurements at $\tau_E = 0$, and to a lesser extent $\tau_E = 0.1$ show a peculiar banding. This banding is associated with an underdamped oscillation and is shown more clearly in Fig. 8. As illustrated in this figure, this short time behavior evolves over hours. The average frequency of this oscillation f_0 (determined by high passing $x(z = 0, t)$ and fitting to a function of the form $x(t) = A \exp(-t/\tau) \sin(2\pi f_0 + \phi)$), across all nine particles was $f_0 = 5610 \pm 50$ Hz. This underdamped oscillation was also observed in experiments conducted:

1. With the $[NaCl] = 0.1$ mM solution substituted with deionised water. Here $f_0 = 5660 \pm 30$ Hz (across two particles), suggesting that f_0 is relatively insensitive to salt concentration.
2. With the trap stiffness increased from 70 to 105 pN/µm. At 70 pN/µm, $f_0 = 5690$ Hz and at $k = 105$ pN/µm, $f_0 = 5680$ Hz (for a single particle), indicating that f_0 is relatively insensitive to trap stiffness.
3. In the chips narrower channels. For the $2W = 1000$ µm channel, $f_0 = 10,100$ Hz and for the $2W = 500$ µm channel, $f_0 = 22,000$ Hz, which along with $2W = 1500$ µm, $f_0 = 5700$ Hz (from above), suggesting that

$$f_0 \approx 1/W$$

.

Over much of the gap, the long time displacement is a quadratic function of z, suggesting that a pressure gradient is present at long times. The displacement x at long times was fitted to Eq. 17, between $-20 \leq z \leq 20$ µm, to determine the offset x_0 and $\Delta\zeta = \zeta_p - \zeta_w$ was computed from Eq. 14. $\Delta\zeta$ values are listed in figure. As can be seen, $\Delta\zeta$ are fairly constant for measurements from the same particle, as could be expected, but differ between measurements from the different samples, indicating that either ζ_p or ζ_w or both are varying between samples. Because $\Delta\zeta > 0$ in all cases, $\zeta_p > \zeta_w$. The force on the particle, which is a superposition of the electroosmotic and electrophoretic forces can be computed from the displacement $x(z, t)$ according to Eq. 11. This force is computed for sample 1 and shown in Fig. 7 16–20.

To decompose the measured force into flow induced electroosmotic and electrophoretic components, ζ_p and ζ_w must be known separately. These parameters were determined by fitting the $x(z, t)$ directly. For each particle, the entire data set ($\tau_E \times t \times z$, $5 \times 2500 \times 50 = 625k$ points) was simultaneously fitted to determine ζ_w and ζ_p, and a pressure a gradient constant c_0. Fitting was performed in MATLAB and made use of COMSOL LiveLink to facilitate communication between MATLAB and COMSOL. Here, test values of ζ_w and the pressure gradient constant were selected in MATLAB, $u(z, t)$ was evaluated for these test values in COMSOL, and, with a test value of ζ_p, $x(z, t)$ was calculated using Eq. 12. This was repeated for each τ_E and the difference between the set of experimental and calculated $x(z, t)$ minimized (in a least-squares sense). Total time to fit each set of data was around 6 h. It became evident that a constant pressure gradient c_0 (see Eq. 16) would not reproduce the short time behavior observed experimentally. Motivated by a literature (van Heiningen et al. 2010) description in which perturbations to electroosmotic flow, due to chip compliance and bubbles, were related to coupling between the pressure gradient and volumetric flow-rate, $U(t)$, it was assumed that:

$$\frac{dp}{dx} = c_U U(t), \tag{19}$$

where $U(t)$ is:

$$U(t) = \frac{2W}{D_h} \int u(z, t) \, dz. \tag{20}$$

This considerably improved the fits. Fits to the data shown Fig. 7 1–5 are shown in Fig. 7 21–25. The fit reproduces the data less well for $\tau_E = 0$ ms. This model will not reproduce
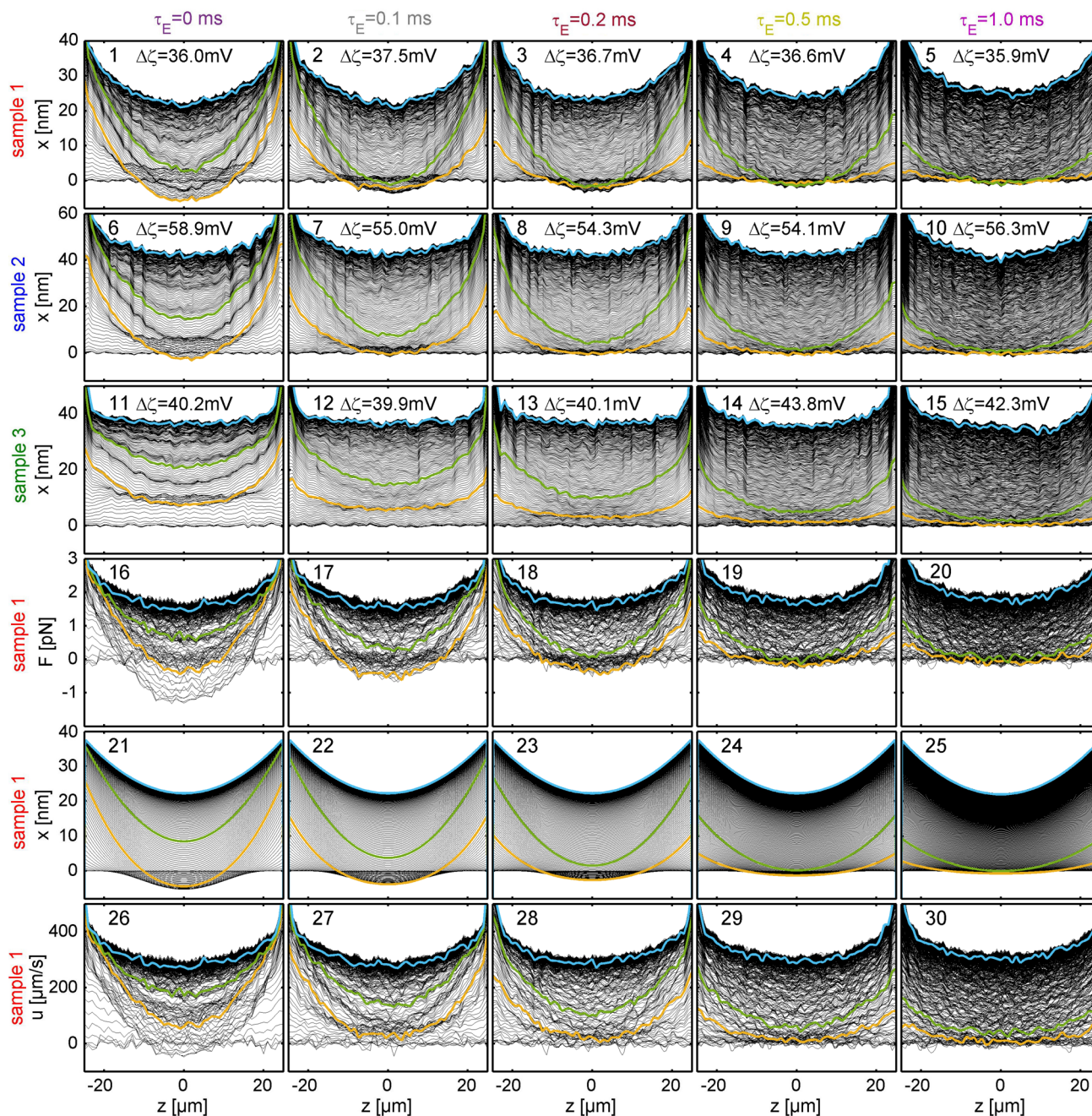
Fig. 7 1–5, 5–10 and 11–15 $x(z, t)$ for three particles with τ_E. 16–20 $F(z, t)$ computed from $x(z, t)$ in 1–5. 21–25 Fit to $x(z, t)$ in 1–5. 26–30 Flow $u(z, t)$ computed from 16–20 with fitted parameters. Data is only shown at $\Delta t = 0.02$ ms increments for clarity

the underdamped oscillation seen experimentally and this discrepancy could be expected.

For the data shown in Fig. 7 1–5 fitted $\zeta_p = -14.4$ mV and $\zeta_w = -55.6$ mV. With ζ_p determined, flow was determined from $F(z, t)$ shown in Fig. 7 16–20 according to:

$$u(z, t) = F(z, t) - \gamma_0 (\varepsilon \zeta_p / \eta) E(t). \tag{21}$$

and is shown in Fig. 7 26–30. Note that the total flow here includes both electroomostic and pressure gradient induced flow.

Fitted parameters are summarized in Fig. 9a. $\Delta\zeta$ for both the fit to the long time behavior and full data set are included. These values are very comparable. The average fitted $\zeta_w = -46.8 \pm 15.0$ mV value is broadly consistent with values reported in the literature for a glass/water interface in [NaCl] = 0.1 mM. The average fitted $\zeta_p = +2.2 \pm 15.7$ mV
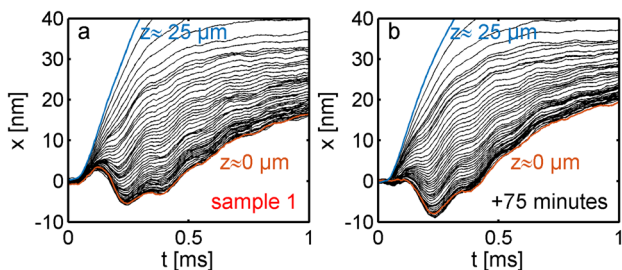
Fig. 8 a, **b** Time evolution of the short time behavior observed over 75 min ($\tau_E = 0$ ms)
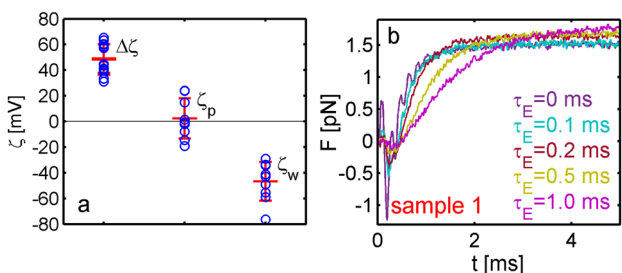

Fig. 9 a Summary of fitted $\Delta\zeta$, $\Delta\zeta_p$ and $\Delta\zeta_w$ values, **b** Mid-gap force for sample 1

value is considerably higher than that expected in [NaCl] = 0.1 mM solution (Yan et al. 2006; Sureda et al. 2012; Miller et al. 2015). Figure 9b shows the mid-gap force $F(z \approx 0, t)$ for sample 1 (see Fig. 7). While results in short time and smaller τ_E are potentially ambiguous because of the underdamped oscillation, the data at short times and larger τ_E are less so: the large negative force predicted for a considerably lower ζ_p is absent in our data.

5 Discussion

The analysis given here presupposes that transient effects associated with the frequency dependence of inertia of the displaced fluid and the particle's electrophoretic mobility can be neglected. It might be speculated that the underdamped oscillation observed at short times is somehow due to this frequency dependence, and that the assumption that we can neglect these effects is questionable. Both of these effects are fairly local to the particle and would not be expected to vary when the channel width W changes. However, we observed a significant increase in the frequency of oscillation when the channel width was decreased which suggests that the oscillation is not due to these local effects. Furthermore, if the oscillation was due to the frequency dependence of the particle's electrophoretic mobility, electrolyte concentration could be expected to influence behavior; we observed no

significant change to the short time behaviour when the salt solution was replaced with deionized water.

At long times, and in all cases, the channel flow profile shows a quadratic dependence on the z-position which suggests a pressure gradient induced back-flow is present and this is explicitly included in our model. The pressure difference across the geometry required to produce the back-flow velocities observed in the channel is around $\Delta p = 2-10$ Pa. Back-flow could be expected if the volume of fluid entering the 5 mm diameter reservoir significantly modified the relative height of the fluid or, perhaps, modified the curvature of the meniscus of the fluid in the reservoir. The total volume of fluid entering the reservoir in the 12.5 ms duration of each voltage step is $V \approx 300 \, \mu\text{m/s} \times 1500 \, \mu\text{m} \times 50 \, \mu\text{m} \times 12.5 \, \text{ms} \approx 0.3$ nL. This volume is very small and would seem to preclude these explanations. Flow into a restriction/constriction could also be expected to produce a pressure gradient induced back-flow. It may be that bubbles, produced by residual degassing of the solution and pinned to the walls of the channel are restricting flow and that variations in bubble sizes are producing the long time differences between samples. It seems possible to test this by extending the 2D numerical model described here to 3D, and to compare the measured flow to that calculated when restrictions are present. This calculation could potentially inform on the apparent dependence of the pressure gradient on the volumetric flow-rate observed in the experimental data.

An underdamped oscillation can be introduced into the flow behavior by including higher order derivatives in the pressure gradient term:

$$\frac{dp}{dx} = c_U U(t) + c_{U'} \frac{dU(t)}{dt} + c_{U''} \frac{d^2 U(t)}{dt^2}. \tag{22}$$

The parameters $c_{U'}$ and $c_{U''}$ can be calculated from (fitted) c_U and estimated oscillation frequency f_0 and characteristic damping time ($\tau \approx 0.3$ ms). The resulting underdamped oscillation does not reproduce behavior observed experimentally. A better model for the observed experimental behavior is:

$$\frac{dp}{dx} = c_U U(t) + \frac{\eta}{E_0 D_h} \text{BP} \left[\frac{dE(t)}{dt}, A, f_0, \Delta f_0 \right] \tag{23}$$

where BP is a recursive bandpass filter (Smith 1997) with amplitude A, center frequency f_0 and bandwidth Δf_0 which acts on the time derivative of the electric field. Using fitted c_u and f_0, the parameters A and Δf_0 were estimated by comparing the experimental normalized volumetric flow-rate $U(t)/U_0$, where U_0 is the volumetric flow-rate at long times, with that calculated. Figure 10a shows a comparison between experimental $U(t)/U_0$, $U(t)/U_0$ calculated without the bandpass term and with the bandpass for a common set
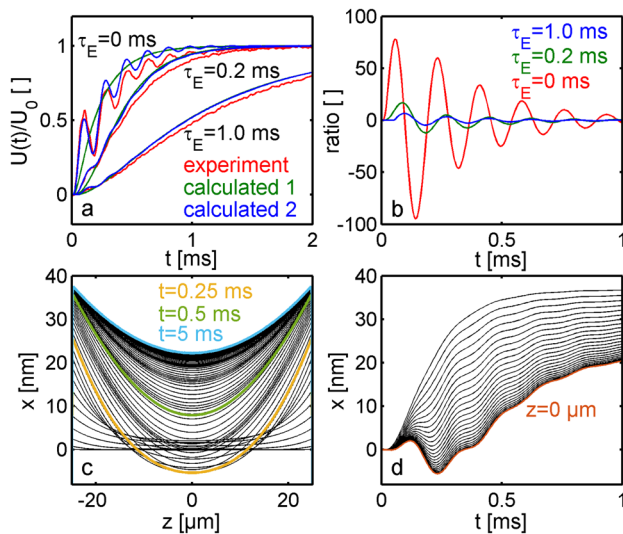
Fig. 10 a Comparison of the calculated effect of the bandpass filter on volumetric flow-rate with experiment. **b** Relative contribution of bandpass term to the pressure gradient. **c, d** Calculated $x(z, t)$ with inclusion of bandpass term in the pressure gradient

of A and Δf_0 values. The inclusion of the bandpass term considerably improves the comparison for small τ_E. Figure 10b shows the ratio:

$$\text{ratio} = \frac{\eta/(E_0 D_h)\text{BP}\left[dE/dt, A, f_0, \Delta f_0\right]}{c_U U_0}, \tag{24}$$

to indicate the relative contribution of each of the terms in Eq. 23. Clearly, the contribution of the bandpass term is most pronounced at short times and small τ_E. Figure 10c, d shows x calculated according to Eq. 23 and with parameters chosen in Fig. 10a. This model reproduces the banding/oscillation observed experimentally at short times. While it is not clear whether this model has physical significance, it may be a useful way of parameterizing the data. Perhaps more significantly, the underdamped oscillation that we observed in this commercial set-up can potentially mask other short time excitations produced by a rapidly time-varying field. This may need to be considered if these excitations are the subject of interest.

While the zeta potential of the glass channel walls, ζ_p, is consistent with that reported in the literature, the zeta potential of the particles, ζ_p, used here, appears considerably higher than that observed in similar experiments. Our results appear to be self-consistent and unambiguous: the particle is displaced significantly in the direction of the field at long times in all cases. This can only occur if the electroosomotic force on the particle is greater than the electrophoretic force (which is reflected in the $\Delta\zeta$ value measured) and indicates that $\zeta_p \gg \zeta_w$. Anomalous behavior has been reported for the zeta potential of polystyrene particles; measurements with

varying electrolyte concentration indicate that the particle's zeta potential exhibits a minimum increasing towards zero at very low electrolyte concentrations (below 1–10 mmol) (Tuin et al. 1995; Folkersma et al. 1998). This anomalous effect was attributed to surface conductance and the presence of a hairy layer on the surface of the particles (Folkersma et al. 1998). The electrolyte concentration used in the study presented here, is in this very low concentration regime and the difference between the zeta potential of the particles measured here and elsewhere may be due to differences in surface conductivity and hairiness of the particles used. While the walls of the micro channel were rejuvenated using an [NaOH] = 1 M solution, following a protocol adapted for cleaning CE capillaries, the polystyrene beads themselves were used without rigorous cleaning. The beads are supplied by the manufacturer in a surfactant solution, to prevent aggregation, and it is conceivable that residual surfactant (or perhaps something else) is contaminating the surface and influencing the particles zeta potential. Because of the variation observed in measurements between particles, and in time, we focused on a single salt concentration here; measurements at other electrolyte concentrations and with cleaning might help to better understand differences between ζ_p measured here, and elsewhere.

6 Conclusion

The displacement due to electroosmotic and electrophoretic forces on an optically trapped particle at start-up were profiled across the channel of a commercial microfluidic chip. Results were inverted to compute the force on the particle and the transient displacement fitted to a FEM model to determine the zeta potential of the walls and particle, and flow. Fits to data indicated that the electroosmotic flow was accompanied by a pressure gradient induced back flow and that while the zeta potential of the walls were consistent with literature values, the zeta potential of the particles were higher than might be expected, which was attributed to differences in surface conditions of the particular particles used.

References

Aris R (1956) On the dispersion of a solute in a fluid flowing through a tube. Proc R Soc Lond A 235:67–77

Berg-Sørensen K, Flyvbjerg H (2014) Power spectrum analysis for optical tweezers. Rev Sci Instrum 75:594–612

Chang CC, Wang C-Y (2008) Starting electroosmotic flow in an annulus and in a rectangular channel. Electrophoresis 29:2970–2979

Folkersma R, van Diemen AJG, Stein HN (1998) Electrophoretic properties of polystyrene spheres. Langmuir 14:5973–5976

Hansen PM, Dreyer JK, Ferkinghoff-Berg J, Oddershede L (2005) Novel optical and statistical methods reveal colloid-wall interactions inconsistent with DLVO and Lifshitz theories. J Colloid Interface Sci 287:561–571

Hunter RJ (2001) Foundations of colloid science. Oxford University Press Inc., New York

Jones PH, Marago OM, Volpe G (2015) Optical tweezers: principles and applications. Cambridge University Press, Cambridge

Kahl V, Gansen A, Galneder R, Rädler JO (2009) Microelectrophoresis in a laser trap: a platform for measuring electrokinetic interactions and flow properties within microstructures. Rev Sci Instrum 80:073704

Keh HJ, Tseng HC (2001) Transient electrokinetic flow in fine capillaries. J Colloid Interface Sci 242:450–459

Kirby BJ (2010) Micro- and nanoscale fluid mechanics: transport in microfluidic devices. Cambridge University Press, Cambridge

Marcos Yang C, Wong TN, Ooi KT (2004) Dynamic aspects of electroosmotic flow in rectangular microchannels. Int J Eng Sci 42:1459–1491

Miller A, Villegas A, Diez FJ (2015) Characterization of the startup transient electrokinetic flow in rectangular channels of arbitrary dimensions, zeta potential distribution, and time-varying pressure gradient. Electrophoresis 36:692–702

Nge PN, Rogers CI, Woolley AT (2013) Advances in microfluid materials, functions, integration, and applications. Chem Rev 113:2550–2583

Raudsepp A, Griffiths M, Sutherland-Smith AJ, Williams MAK (2015) Developing a video tracking method to study interactions between close pairs of optically trapped particles in three dimensions. Appl Opt 54:9518–9527

Raudsepp A, Kent LM, Hall SB, Williams MAK (2018) Overstretching partially alkyne functionalized dsDNA using near infrared optical tweezers. Biochem Biophys Res Commun 496:975–980

Semenov I, Otto O, Stober G, Papadopoulos P, Keyser UF, Kremer F (2009) Single colloid electrophoresis. J Colloid Interface Sci 337:260–264

Smith SW (1997) The scientist and engineer's guide to digital signal processing. California Technical Publishing, San Diego

Sureda M, Miller A, Diez FJ (2012) In situ particle zeta potential evaluation in electroosmotic flows from time-resolved microPIV measurements. Electrophoresis 33:2759–2768

Tang G, Yan D, Yang C, Gong H, Chai JC, Lam YC (2006) Assessment of joule heating and its effects on electroosmotic flow and electrophoretic transport of solutes in microfluidic channels. Electrophoresis 27:628–639

Tuin G, Sender JHJE, Stein HN (1995) Electrophoretic properties of monodisperse polystyrene particles. J Colloid Interface Sci 179:522–531

van Heiningen JA, Mohammadi A, Hill RJ (2010) Dynamic electrical response of colloidal micro-spheres in compliant micro-channels from optical tweezers velocimetry. Lab Chip 10:1907–1921

Yan D, Nguyen NT, Yang C, Huang X (2006) Visualizing the transient electroosmotic flow and measuring the zeta potential of microchannels with a micro-PIV technique. J Chem Phys 124:021103

Zhao C, Zhang W, Yang C (2017) Dynamic electroosmotic flows of power-law fluids in rectangular microchannels. Micromachines 8:34